

## Article

# Montbrayite from the Svetlinsk Gold–Telluride Deposit (South Urals, Russia): Composition Variability and Decomposition

Olga V. Vikent'eva <sup>1,\*</sup> , Vladimir V. Shilovskikh <sup>2</sup> , Vasily D. Shcherbakov <sup>3</sup>, Tatyana N. Moroz <sup>4</sup>, Ilya V. Vikentyev <sup>1</sup>  and Nikolay S. Bortnikov <sup>1</sup>

<sup>1</sup> Institute of Geology of Ore Deposits, Petrography, Mineralogy and Geochemistry, Russian Academy of Sciences (IGEM RAS), 119017 Moscow, Russia; viken@igem.ru (I.V.V.); bns@igem.ru (N.S.B.)

<sup>2</sup> Geomodel Center, St. Petersburg State University (SPbU), 199034 St. Petersburg, Russia; vvshlvskh@gmail.com

<sup>3</sup> Faculty of Geology, Lomonosov Moscow State University, 119991 Moscow, Russia; vasily7@gmail.com

<sup>4</sup> Sobolev Institute of Geology and Mineralogy, Siberian Branch of the Russian Academy of Sciences (IGM SB RAS), 630090 Novosibirsk, Russia; moroz@igm.nsc.ru

\* Correspondence: ovikenteva@rambler.ru; Tel.: +7-499-230-82-59

**Abstract:** A rare gold–telluride montbrayite from the large Svetlinsk gold–telluride deposit (South Urals, Russia) was comprehensively studied using optical microscopy, scanning electron microscopy, electron microprobe analysis, reflectance measurements, electron backscatter diffraction, and Raman spectroscopy. Significant variations in the composition of the mineral were revealed (in wt%): Au 36.98–48.66, Te 43.35–56.53, Sb 2.49–8.10, Ag up to 4.56, Pb up to 2.04, Bi up to 0.33, Cu up to 1.42. There are two distinct groups with much more-limited variation within the observed compositional interval (in wt%): (1) Au 36.98–41.22, Te 49.35–56.53, Sb 2.49–5.57; (2) Au 47.86–48.66, Te 43.35–44.92, Sb 7.15–8.10. The empirical formula calculated on the basis of 61 *apfu* is  $\text{Au}_{16.43-23.28}\text{Sb}_{1.79-6.09}\text{Te}_{32.01-38.89}\text{Ag}_{0-3.69}\text{Bi}_{0-0.14}\text{Pb}_{0-0.90}\text{Cu}_{0-1.96}$ . Two substitution mechanisms for antimony are proposed in the studied montbrayite grains: Sb→Au (2.5–5.6 wt% Sb) and Sb→Te (7–8 wt% Sb). The dependence of the reflection spectra and Raman spectra on the antimony content and its substitution mechanism, respectively, was found in the mineral. The slope of the reflectance spectra decreases and the curve in the blue–green region of the spectrum disappears with increasing Sb content in montbrayite. Raman spectra are reported for the first time for this mineral. The average positions of the peak with high-intensity are  $\sim 64\text{ cm}^{-1}$  and  $\sim 90\text{ cm}^{-1}$  for montbrayite with Sb→Te and Sb→Au, respectively. Two grains of montbrayite demonstrate decomposition according to two schemes: (1) montbrayite (7 wt% Sb) → native gold + calaverite ± altaite, and (2) montbrayite (5 wt% Sb) → native gold + tellurantimony ± altaite. A combination of melting and dissolution–precipitation processes may be responsible for the formation of these decomposition textures.

**Keywords:** montbrayite; gold tellurides; Au–Sb–Te system; decomposition; EBSD; Raman spectroscopy; Svetlinsk gold deposit; Urals



**Citation:** Vikent'eva, O.V.; Shilovskikh, V.V.; Shcherbakov, V.D.; Moroz, T.N.; Vikentyev, I.V.; Bortnikov, N.S. Montbrayite from the Svetlinsk Gold–Telluride Deposit (South Urals, Russia): Composition Variability and Decomposition. *Minerals* **2023**, *13*, 1225. <https://doi.org/10.3390/min13091225>

Academic Editor: Huan Li

Received: 26 August 2023

Revised: 14 September 2023

Accepted: 16 September 2023

Published: 18 September 2023



**Copyright:** © 2023 by the authors. Licensee MDPI, Basel, Switzerland. This article is an open access article distributed under the terms and conditions of the Creative Commons Attribution (CC BY) license (<https://creativecommons.org/licenses/by/4.0/>).

## 1. Introduction

Montbrayite as a new mineral species was first described at the Robb-Montbray mine, Montbray, Abitibi County, Quebec (Canada) [1]. The chemical formula of the mineral was given as  $\text{Au}_2\text{Te}_3$ , or  $(\text{Au,Sb})_2\text{Te}_3$ , and other elements (Ag, Pb, Bi) reported in the chemical analysis were excluded because the studied montbrayite contained inclusions of tellurobismuthite ( $\text{Bi}_2\text{Te}_3$ ), altaite ( $\text{PbTe}$ ), and petzite ( $\text{Ag}_3\text{AuTe}_2$ ). This montbrayite contained 1 wt% Sb.

Attempts to synthesize  $\text{Au}_2\text{Te}_3$ , reported by [1–4] as the mineral montbrayite, were unsuccessful. Rucklidge [5] first suggested that montbrayite should contain “small but probably essential amounts of Bi and Pb” to be stabilized. Later, the experiments of Bachechi [6] allowed him to conclude that montbrayite is not stable in the Au–Te system; however,

isomorphous substitution of Bi, Pb, and Sb or of Sb only was responsible for the stability of montbrayite. Then, Gather and Blachnik [7,8], who studied the ternary Au–Sb–Te system found a new ternary compound of the approximate composition  $\text{AuSb}_{0.07}\text{Te}_2$ ; the X-ray diagram of this phase corresponds to the montbrayite from [1]. Later, Nakamura and Ikeda [9] studied the ternary phase relations in the Au–Sb–Te system at 350 °C and also found the  $\text{Au}_{1.9}(\text{Te}_{2.64}\text{Sb}_{0.46})_{3.1}$  phase, whose XRD pattern is most similar to that of montbrayite reported by [6]. Synthetic montbrayite shows a small solid solution field and has non-stoichiometric composition, which is located near the  $\text{Au}_2(\text{Te,Sb})_3$  stoichiometric line, but not on the  $(\text{Au,Sb})_2\text{Te}_3$  line [9]. Around the same time, Shackleton and Spry [10], studying Sb-rich montbrayite from the Golden Mile, Western Australia, concluded that Bi, Ag, and Pb appear to stabilize montbrayite in much the same manner as Sb. They also assumed a modification of the formula of montbrayite to  $(\text{Au,Ag,Sb})_2(\text{Te,Sb,Bi})_3$  or, more likely,  $(\text{Au,Ag,Sb,Bi})_2(\text{Te,Sb,Bi})_3$  [10].

However, to determine the formula correctly, it is necessary to study the structure of the mineral. The first X-ray diffraction data were obtained for the first finding of montbrayite, but the crystal structure remained unsolved [1]. Attempts to solve the montbrayite structure were made by Bachechi [11] and Edenharter with colleagues [12]. Later, the crystal structure of the mineral was solved for montbrayite from the Robb-Montbray mine [13]. The authors suggested a possible scenario: (1) Pb can substitute for Au or Te; (2) Bi can substitute for Te (in an ordered fashion) or Au; (3) Sb can substitute for Au (in a disordered fashion) or Te; (4) Ag, when present, substitutes for Au. On the basis of the structural and chemical data, the chemical formula of montbrayite was revised and was approved by the Commission on New Minerals as  $(\text{Au,Ag,Sb,Bi,Pb})_{23}(\text{Te,Sb,Bi,Pb})_{38}$  [13].

Despite the fact that the mineral was discovered about 80 years ago, its findings are documented only in a few deposits. Antimony-rich (Golden Mile, Western Australia [10,14–16]; Enasen, central Sweden [17]), Bi-rich (Robb-Montbray mine, Quebec, Canada [1,5,6,13,18], Kochkar, S. Urals, Russia [19]), and Pb-rich (Zhana-Tyube, South Aksu, Zholymbet, Kazakhstan [20]) montbrayite were found in the ores of the gold deposits. Bi-rich montbrayite was also defined in a sample of noritic breccias from the Voronezhsky massif [21]. Montbrayite is still a rare gold telluride, but it is one of the main gold minerals [22].

In this paper, Sb-rich montbrayite from the Svetlinsk deposit was comprehensively studied using optical microscopy, scanning electron microscopy (SEM), electron microprobe analysis (EMPA), reflectance measurements, electron backscatter diffraction (EBSD), and Raman spectroscopy (RS). In addition, montbrayite decomposition was first found, and we tried to explain the formation mechanism of these decomposition textures. The new information on montbrayite, a rare mineral with a chemical variability of composition, will be useful for mineralogists studying the mineralogy and genesis of telluride-bearing gold deposits.

## 2. Geological Setting

The large (~135 t Au) gold–telluride Svetlinsk deposit (54°17' N, 60°25' E) is located within the East Uralian megazone at the junction of the Kochkar anticlinorium with the Aramil-Sukhtel synclinorium [23]. Host Devonian–Carboniferous volcano–sedimentary rocks underwent strong up to amphibolite facies metamorphism caused by emplacement of a hidden granitic pluton and by the influence of a major west-dipping thrust-fault [23]. Gold mineralization is represented by disseminated sulfides in the host rocks ( $C_{\text{Au}}$  up to 1 g/t) and by sulfide–quartz veins ( $C_{\text{Au}} = 0.8\text{--}2.5$  g/t). Three mineralization stages have been recognized [23,24]: (1) the disseminated quartz–pyrite–pyrrhotite stage, with rare chalcopyrite, tetrahedrite, galena, and native gold; (2) the quartz–pyrite vein stage, with scheelite; (3) the gold–telluride stage (the main productive one). Native gold (620–965‰) is often associated with tellurides that are common and varied in the ore veins. Tellurides of Fe, Ni, Pb, Sb, Bi, Ag, and Au were found in the ore assemblages: frobergite, melonite, altaite, tellurantimony, vavřinite, tsumoite, tellurobismuthite, tetradymite, volynskite, montbrayite, calaverite, sylvanite, krennerite, petzite, hessite, empressite. Tellurides form simple or more often complex inclusions in quartz and also fill fractures in it and are rarely

intergrown with pyrite, chalcopyrite, and tetrahedrite. Mineralization is accompanied by quartz–sericite, quartz–carbonate–sericite (beresite, listvenite), quartz–albite, quartz–microcline, and quartz–biotite hydrothermal alteration. Previous studies have shown the ore to be polygenetic, involving contrasting fluids with multiple sources [23,25,26]. A specific feature of the deposit is the high formation temperature of the mineral assemblages including those containing some tellurides.

### 3. Materials and Methods

Montbrayite was found in specimens that were taken from the open pit (levels 275–300 m) of the deposit. Polished samples were studied under a polarizing microscope Olympus BX-51 and a JEOL JSM-5610LV scanning electron microscope equipped with an Oxford-INCA-450 EDS at the Institute of Geology of Ore Deposits, Petrography, Mineralogy and Geochemistry, Russian Academy of Sciences (IGEM RAS).

The chemical composition was determined at the IGEM RAS using a JEOL JXA-8200 electron microprobe equipped with five wavelength-dispersive spectrometers (WDS) and operated at 20 kV and 20 nA. The beam diameter was 1  $\mu\text{m}$ . Calibration standards (X-ray lines, analyzing crystals) included AuTe<sub>2</sub> for Au ( $M\alpha$ , PETH) and Te ( $L\alpha$ , PETH), Sb<sub>2</sub>S<sub>3</sub> for Sb ( $L\alpha$ , PETH), AgSbS<sub>2</sub> for Ag ( $L\alpha$ , PETH), Bi<sub>2</sub>Te<sub>3</sub> for Bi ( $M\beta$ , PETH), PbS for Pb ( $M\alpha$ , PETH), and CdSe for Se ( $L\alpha$ , TAP). The counting times were 10 s on peaks and 5 s on the upper and lower backgrounds for Au, Te, Sb, and Ag; 30 and 15 s for Pb, Cu, and Se; and 60 and 30 s for Bi, respectively. Detection limits ( $3\sigma$  criterion) for the minor elements (wt%) were 0.09 for Ag, 0.06 for Bi and Cu, 0.05 for Pb, and 0.04 for Se. The ZAF correction was performed using the JEOL software.

Reflectance measurements were performed in air relative to a silicon standard with a microscope–spectrophotometer (MSF-R, LOMO) with a photoelectronic multiplier (Hamamatsu, Japan) at the Institute of Mineralogy (Miass, Russia). The lens was  $40 \times 0.65$  (achromat). The diameter of the measuring area was 7  $\mu\text{m}$ .

Electron backscatter diffraction (EBSD) studies were performed simultaneously with EDX mapping on a Hitachi S-3400N scanning electron microscope (SEM) equipped with an Oxford X-Max 20 energy-dispersive X-ray (EDX) spectrometer and NordLys Nano EBSD detector (“Geomodel” resource center, Scientific Park, SPbU). Prior to the EBSD investigation, the samples were polished with progressively smaller diamond suspensions up to 0.25  $\mu\text{m}$  and Ar<sup>+</sup>-plasma-etched (Oxford Instruments Ionfab300, 10 min, incident angle of 45°, accelerating voltage of 500 V, current of 200 mA, beam diameter of 10 cm; “Nanophotonics” resource center, Scientific Park, SPbU). Montbrayite crystals produce high-quality diffraction patterns with an excellent fit to the known montbrayite structure (12 bands, 0.26° MAD, AMCSD 0014682). The conditions for single-pattern acquisition were as follows: 30kV accelerating voltage, 1 nA beam current, 0.2 s dwell time per one image, the averaging of 20 images. No binning was applied. The mapping conditions were the same except  $2 \times 2$  image binning and 2-image averaging. Image processing was automatically performed using the Oxford AzTec software for EBSD image acquisition and matching.

The Raman spectra were collected with a Horiba XPlora (Jobin Yvon) Raman spectrometer installed on an Olympus BX51 optical microscope and equipped with a Si-based charge-coupled detector (CCD) at the Department of Petrology and Volcanology (Faculty of Geology, Lomonosov Moscow State University) using circularly polarized 532 nm excitation wavelength and a diffraction grating of 2400 lines/mm (spectral resolution  $< 1 \text{ cm}^{-1}$ ). The Raman spectra were collected in the range 50–1200  $\text{cm}^{-1}$ . Samples were irradiated for 300 s ( $30 \times 10$  s) with an  $\sim 3$  mW laser beam (25% of maximum laser source power) to prevent mineral surface destruction observed by us at higher laser power. The spatial resolution was approximately 1  $\mu\text{m}$ . Deconvolution of the Raman spectra using a Voigt function was carried out with the Origin7.5 software packet.

## 4. Results

### 4.1. Mineral Assemblages and Physical Properties

Grains of montbrayite were found in several assemblages in the quartz–sulfide veins. Montbrayite occurs as inclusions in quartz and chlorite together with tellurides (tellurides of Fe, Sb, Pb, and, rarely, Au–Ag), native gold, and less often, with sulfides and sulfosalts (Figure 1) and as inclusions (3–5  $\mu\text{m}$ ) in pyrite. The observed montbrayite assemblages can be divided into two groups: (1) montbrayite coexists with frohbergite, as well as native gold, tellurantimony and petzite, which is intergrown with chalcopyrite; intergrowths of native gold with calaverite (or tellurantimony) and altaite were found along the contact of large (about 100  $\mu\text{m}$ ) grains of montbrayite and frohbergite; (2) montbrayite coexists with petzite and sulfosalts (robinsonite and tetrahedrite). In this study, the selected montbrayite grains are indicated by capital letters (from A to J) for the correspondence between microphotographs, electron microprobe analyses in the table and graphs, as well as Raman spectra. Montbrayite was comprehensively studied in the following assemblages: montbrayite (Grain A, 150  $\times$  150  $\mu\text{m}$ ) + native gold (910%) + calaverite + frohbergite  $\pm$  altaite (Figures 1a and 2); montbrayite (Grain B, 90  $\times$  60  $\mu\text{m}$ ) + native gold (962%) + tellurantimony + frohbergite  $\pm$  altaite (Figure 1b); montbrayite (Grain C, up to 10  $\times$  up to 70  $\mu\text{m}$ ) + chlorite + native gold (935%) + tellurantimony + frohbergite (Figure 1c); montbrayite (Grain D, 10  $\times$  10  $\mu\text{m}$ ) + chalcopyrite + native gold (932%) + chlorite + tellurantimony + altaite + frohbergite (Figure 1d); montbrayite (Grain E, 15  $\times$  25  $\mu\text{m}$ ) + petzite + native gold (876%) + tellurantimony + frohbergite + chalcopyrite (Figure 1e); montbrayite (Grain F, 5  $\times$  12  $\mu\text{m}$ ) + petzite + tellurantimony + chalcopyrite (Figure 1f); montbrayite (Grain G, 7  $\times$  10  $\mu\text{m}$ ) + robinsonite + tetrahedrite + petzite (Figure 1g); montbrayite (Grain H, 10  $\times$  10  $\mu\text{m}$ ) + robinsonite + tetrahedrite + petzite + tellurantimony (Figure 1h); montbrayite (Grain I, up to 5  $\times$  up to 7  $\mu\text{m}$ ) + robinsonite + tetrahedrite + petzite (Figure 1i). The inclusion of montbrayite in pyrite is Grain J ( $\sim$ 5  $\mu\text{m}$ ).

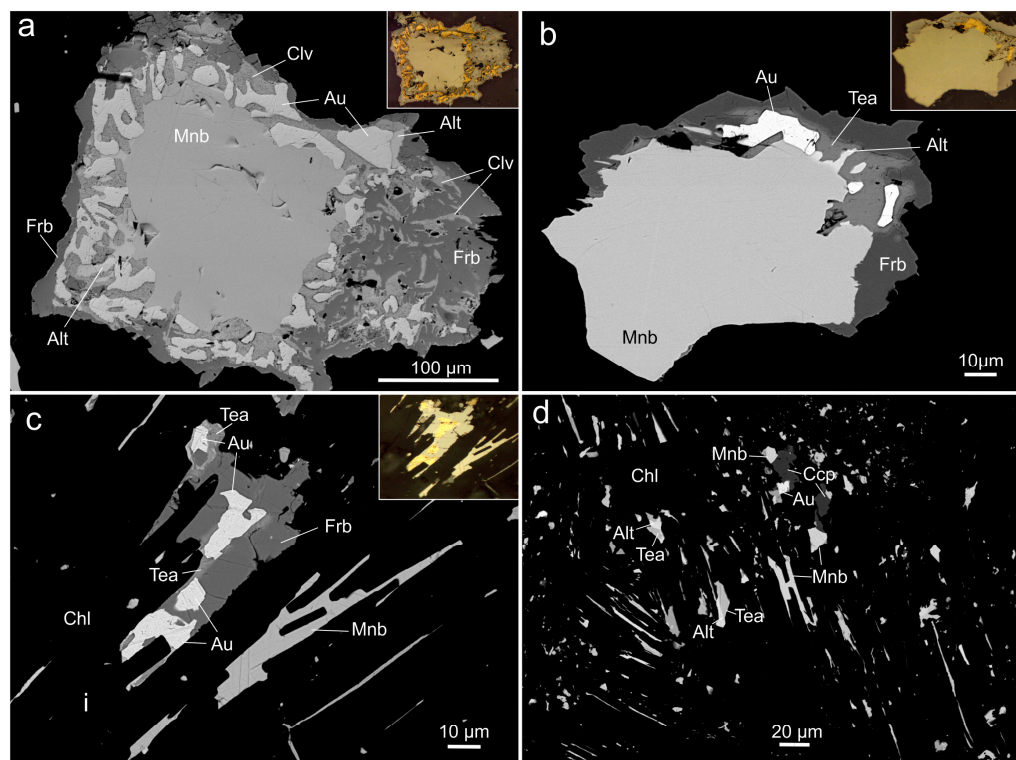
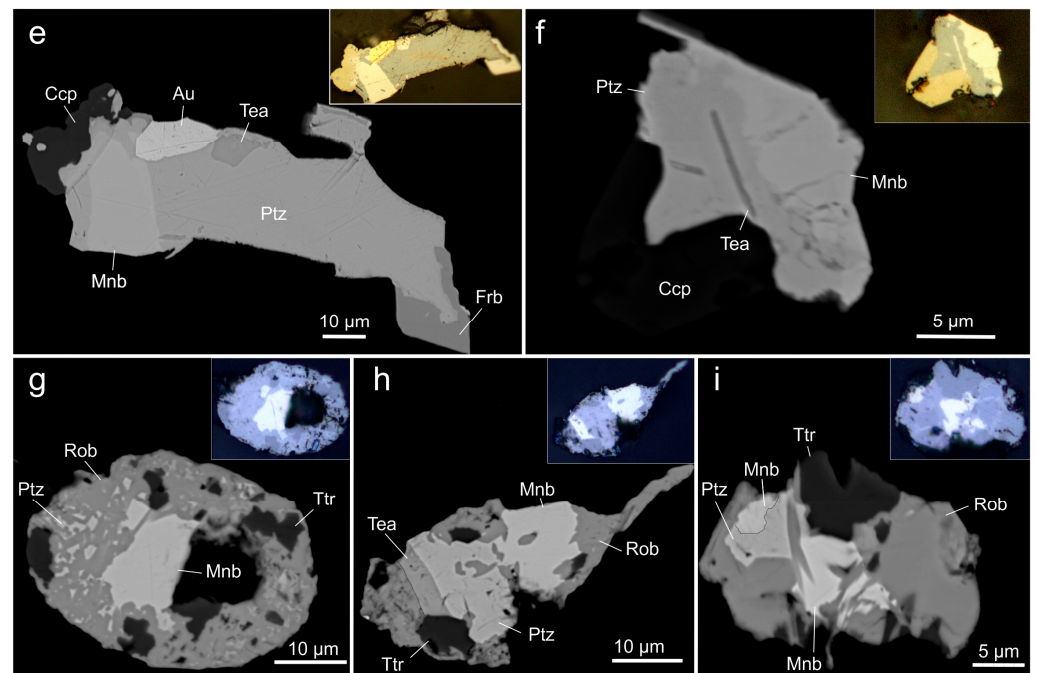


Figure 1. Cont.



**Figure 1.** Backscatter electron (BSE) and reflected light (plane-polarized, in the inset) images showing the montbrayite assemblages from the Svetlinsk deposit. (a) Montbrayite (Grain A) with the rim of eutectoid-like (or symplectite-like) intergrowths of porous calaverite and native gold along the contact with frohbergite. Altaite is rare among calaverite and native gold. See also Figure 2 for this grain. (b) Intergrowth of montbrayite (Grain B) and frohbergite with native gold, tellurantimony, and rare altaite along their contact. The diffusion boundary is between tellurantimony and frohbergite according to the SEM data (profiles and mapping). (c) Montbrayite (Grain C) and intergrowth of frohbergite with native gold and tellurantimony in the chlorite matrix. (d) Montbrayite alone or with chalcopyrite (Grain D), as well as intergrowths of altaite with tellurantimony in chlorite matrix. (e) Montbrayite (Grain E) occurs as inclusion in petzite together with native gold and tellurantimony; petzite is intergrown with frohbergite and chalcopyrite. (f) Montbrayite (Grain F) in contact with petzite intergrown with chalcopyrite. Elongate inclusions of tellurantimony are in petzite. (g) Montbrayite (Grain G) is surrounded by a complex intergrowth of robinsonite with tetrahedrite and petzite. (h) Montbrayite (Grain H) coexists with robinsonite, petzite, tellurantimony, and tetrahedrite. (i) Montbrayite (Grain I) is intergrown with petzite, robinsonite, and tetrahedrite. The matrix is quartz for all images, except for Figure 1c,d. The figure letter number corresponds to the grain designation. Abbreviations: Alt—altaite, Au—native gold, Ccp—chalcopyrite, Chl—chlorite, Clv—calaverite, Frb—frohbergite, Mnb—montbrayite, Ptz—petzite, Rob—robinsonite, Tea—tellurantimony, Ttr—tetrahedrite.

The review of mineral assemblages found for Bi-, Sb-, and Pb-rich varieties of montbrayite is collected in Table 1.

In plane-polarized reflected light, montbrayite is white or creamy white. Under crossed polarizers, the mineral shows moderate anisotropism. However, the variations in the amount of impurities, such as Sb, Bi, Pb, and Ag, result in optical differences for montbrayite [10].

Reflectance data for Sb-rich montbrayite from the Svetlinsk deposit are shown in Figure 3. They were compared with the appropriate spectra for Bi-rich montbrayite from Robb-Montbray (taken from [18]). The spectrum profile changes with increasing Sb content; the slope of the spectra decreases, and the curve in the blue–green region of the spectrum disappears. The significant differences in the dispersion of the reflectance of montbrayite were noted [18].

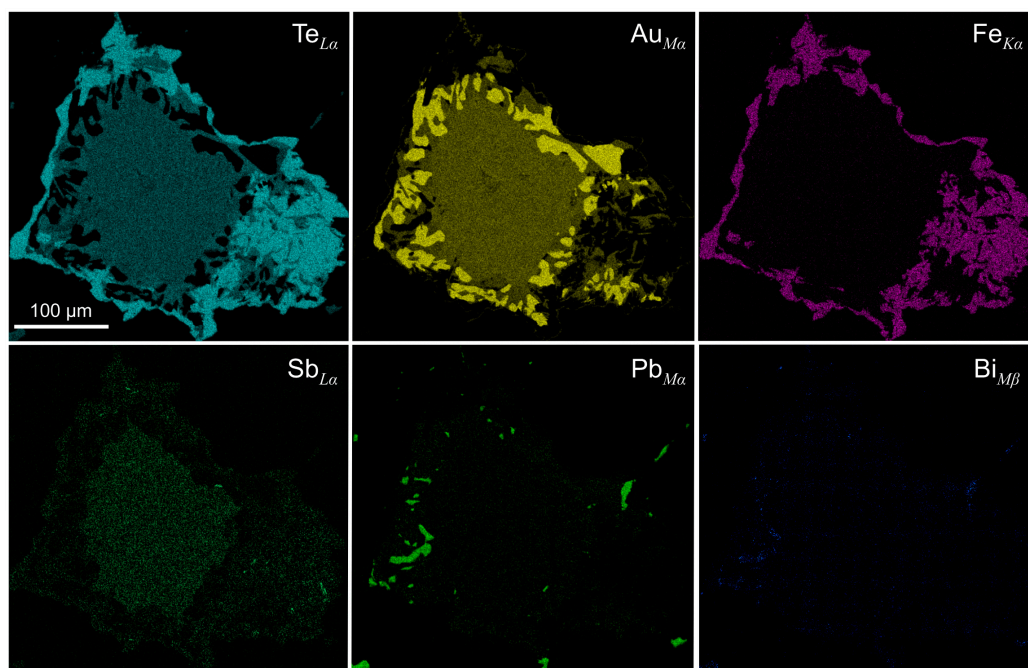


**Figure 2.** EDX element maps of the montbrayite.

**Table 1.** Review of montbrayite mineral assemblages at the gold deposits.

Mnb	Deposit/Location	Mineral Assemblages	References
Bi-rich	Robb-Montbray Mine/Quebec, Canada	Mnb-Au-Tbi-Alt-Ptz-Mlt	[1]
		Mnb-Clv	[5]
		Mnb-Tbi	[18]
		Mnb-Tbi-Frb-Ptz-Alt-Mlt-Ccp-Au	[13]
	Kochkar/S. Urals, Russia	Mnb-Au-Koc	[19]
Sb-rich	Golden Mile/Kalgoorlie, Western Australia	Mnb-Mlt, Mnb-Syl, Mnb-Clv, Mnb-Alt-Ptz	[14]
		Mnb-Alt-Ptz, Mnb-Au, Mnb-Ptz, Mnb-Clv-Au, Mnb-Au-Mtg, Mnb-Au-Tea	[15]
		Mnb-Alt, Mnb-Alt-Ptz, Mnb-Au-Ptz	[27]
		Mnb-Alt-Ptz, Mnb-Au-Ptz	[10]
		Mnb-Au-Mlt, Mnb-Au-Tea, Mnb-Alt-Tea-Clr-Mlt-Clv-Ptz	[16]
	Enasen/Sweden	Mnb-Au-Tea, Mnb-Frb	[17]
	Svetlinsk/S. Urals, Russia	Mnb-Frb-Au-Clv-Alt, Mnb-Frb-Au-Tea-Alt, Mnb-Frb-Au-Tea-Chl-Ccp, Mnb-Frb-Au-Tea-Ptz-Ccp, Mnb-Tea-Ptz-Ccp, Mnb-Tea-Ptz-Rob-Ttr	This study
Pb-rich	Zhana-Tyube, South Aksu, Zholymbet/Kazakhstan	Mnb-Mlt-Frb-Au in the pyrrhotite ores	[20]

Abbreviations: Alt—altaite, Au—native gold, Ccp—chalcocopyrite, Chl—chlorite, Clr—coloradoite, Clv—calaverite, Frb—frohbergite, Hes—hessite, Koc—kochkarite, Mlt—melonite, Mnb—montbrayite, Mtg—mattagamite, Ptz—petzite, Rob—robinsonite, Syl—sylvanite, Tbi—tellurobismuthite, Tea—tellurantimony, Ttr—tetrahedrite.

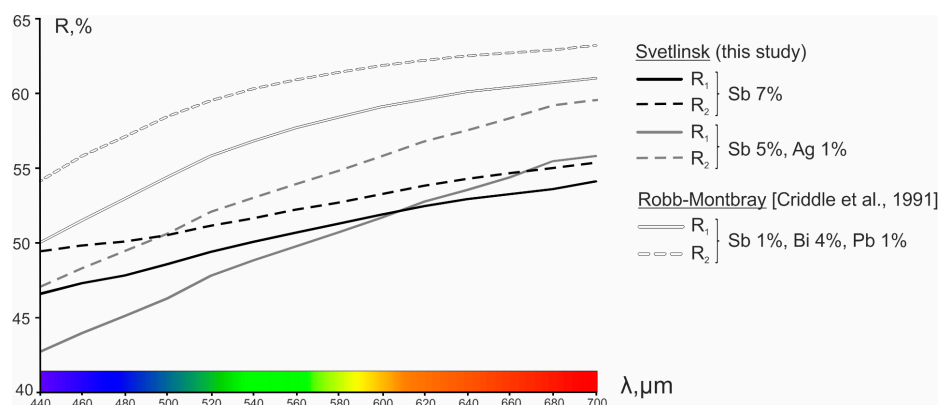


**Figure 3.** Reflectance spectra for montbrayite with varying contents of antimony and other impurities (in wt%) from the Svetlinsk (Grain A, 7 wt% Sb, and Grain B, 5 wt% Sb) and Robb-Montbray [18].

4.2. Chemical Composition

Electron microprobe analyses of montbrayite from the Svetlinsk deposit are given in Table 2. Significant variations were detected in the composition of the mineral (in wt%): Au 36.98–48.66, Te 43.35–56.53, Sb 2.49–8.10, Ag up to 4.56, Pb up to 2.04, Bi up to 0.33, Cu up to 1.42. There are two distinct groups with much more-limited variation within the observed compositional interval (in wt%): (1) Au 36.98–41.22, Te 49.35–56.53, Sb 2.49–5.57; (2) Au 47.86–48.66, Te 43.35–44.92, Sb 7.15–8.10. The empirical formula calculated on the basis of 61 apfu is  $Au_{16.43-23.28}Sb_{1.79-6.09}Te_{32.01-38.89}Ag_{0-3.69}Bi_{0-0.14}Pb_{0-0.90}Cu_{0-1.96}$ . Variations in the chemical composition of montbrayite are shown in Figure 4 together with results for both montbrayite from other gold deposits and the synthetic phase from the literature. On the Au vs. Te (in apfu) graph (Figure 4c,d), all the analyses were divided into two groups. We believe this was caused by different substitution mechanisms for antimony mainly: in one group, antimony substitutes predominantly for gold (Sb→Au, all grains studied, except Grain A), in the other—predominantly for tellurium (Sb→Te, Grain A, and literature data). An inverse relationship between Sb and Ag contents in grains from the first group indirectly confirms the Sb→Au mechanism because Ag, when present, substitutes for Au [13]. The same grains contain minor Cu.

**Table 2.** Electron microprobe analyses of montbrayite from the Svetlinsk deposit.

No.	wt.%							Formula Calculated on the Basis of 61 Atoms							
	Ag	Au	Cu	Pb	Sb	Bi	Te	Total	Ag	Au	Cu	Pb	Sb	Bi	Te
1	—	48.66	—	0.26	7.22	—	43.35	99.49	0	23.28	0	0.12	5.59	0	32.01
2	—	48.47	—	0.23	7.15	—	43.39	99.24	0	23.24	0	0.10	5.54	0	32.12
3	—	47.88	—	0.22	7.15	—	43.50	98.75	0	23.03	0	0.10	5.57	0	32.30
4*	—	48.19	—	0.61	8.10	—	44.92	101.82	0	22.40	0	0.27	6.09	0	32.24
5*	—	47.86	—	—	7.79	—	44.14	99.79	0	22.70	0	0	5.98	0	32.32
6*	—	48.62	—	0.34	7.88	—	44.71	101.55	0	22.69	0	0.15	5.95	0	32.21
7	0.93	41.16	0.38	—	4.95	—	52.95	100.37	0.77	18.77	0.54	0	3.65	0	37.27
8	0.97	40.99	0.47	—	5.02	—	53.29	100.74	0.81	18.58	0.65	0	3.68	0	37.28
9	0.96	41.22	0.39	—	5.08	—	53.11	100.76	0.79	18.71	0.55	0	3.73	0	37.21
10	2.36	39.19	0.46	—	3.79	0.11	55.42	101.33	1.92	17.49	0.63	0	2.73	0.05	38.17
11	1.54	37.69	0.96	—	5.15	—	55.06	100.40	1.26	16.80	1.33	0	3.71	0	37.90
12	1.36	39.34	1.16	—	4.07	0.33	53.47	99.73	1.13	17.80	1.63	0	2.98	0.14	37.34
13	1.19	38.90	1.42	—	4.25	0.32	54.89	100.97	0.96	17.27	1.96	0	3.05	0.14	37.62
14	2.22	39.83	0.47	—	3.78	0.33	52.93	99.56	1.85	18.20	0.67	0	2.80	0.14	37.34
15	1.60	39.58	0.30	—	4.38	—	52.58	98.44	1.35	18.34	0.42	0	3.28	0	37.61
16	4.56	37.18	0.16	0.09	2.52	—	56.53	101.04	3.69	16.50	0.22	0.04	1.81	0	38.74
17	4.42	37.18	0.11	—	2.49	—	56.53	100.73	3.60	16.57	0.15	0	1.79	0	38.89
18	2.48	38.81	0.26	2.04	5.57	—	49.35	98.50	2.10	18.03	0.37	0.90	4.19	0	35.40
19*	4.03	36.98	—	—	3.86	—	55.13	100.00	3.31	16.63	—	—	2.81	—	38.26

Notes: dash—below detection limit, blank—not analyzed, \*—SEM analyses, all others by EMPA. Analyses 1–6 are for Grain A, 7–9 for B, 10 for C, 11 for D, 12–14 for E, 15 for F, 16 for G, 17 for H, 18 for I, 19 for J. The Se content was below the detection limit in all analyses.

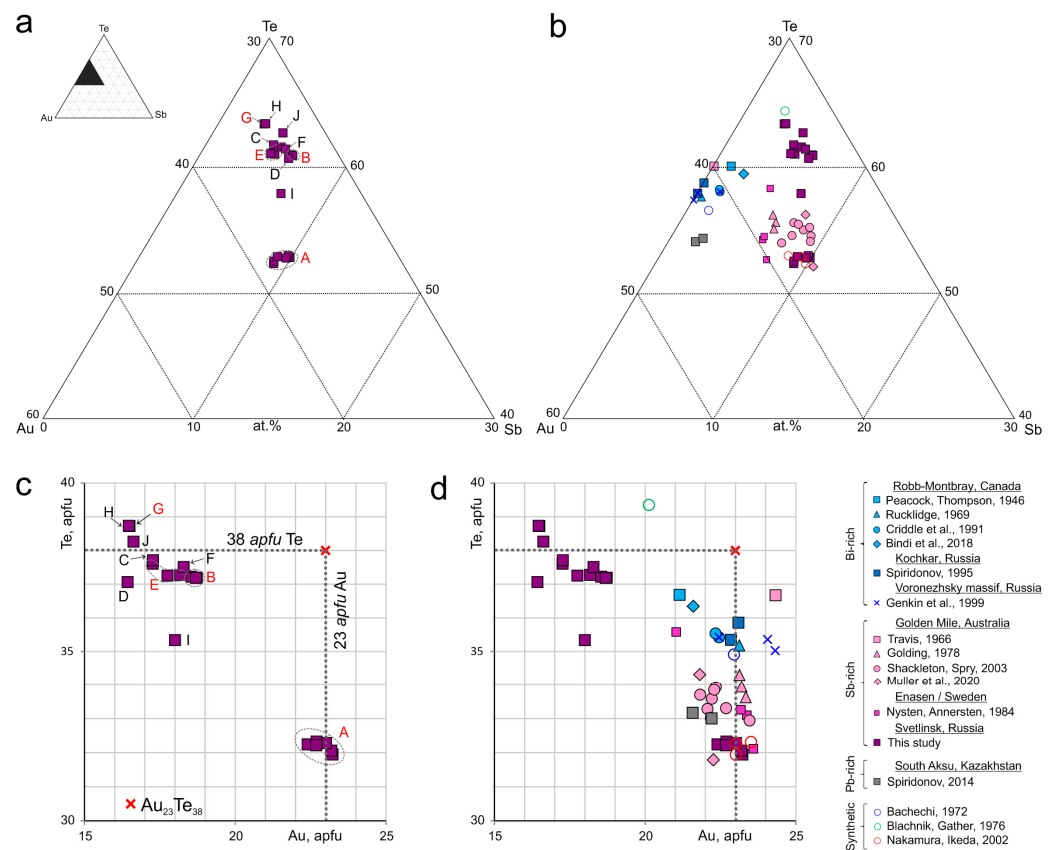


**Figure 4.** Chemical composition variations of montbrayite from the Svetlinsk deposit in comparison with the literature data [1,5,6,8–10,13–21,28]. (a,b) Au–Sb–Te ternary diagram. The black triangular area has been enlarged. (c,d) Au vs. Te (in *apfu*) graph. Capital letters indicate studied grains; the grains with EBSD data are highlighted in red. The structure refinement was made for the composition from [13]. See the chemical analyses in Tables 2 and A1.

#### 4.3. EBSD Study

The EBSD study showed a perfect consistency of the studied grains (A, B, E, and G) with the structure of montbrayite. EBSD mapping of the montbrayite-containing assemblage is shown on the example Grain A (Figure 5). Different phases and crystallites do not have pronounced orientation relationships. The montbrayite core is a single crystal. It is surrounded by randomly oriented native gold grains up to several tens of micrometers in size. However, individual particles are mainly one crystal only. Frohbergite is also represented by misoriented crystallites of 1–100  $\mu\text{m}$ . The quartz matrix consists of macroscopic grains, each of which twins about the *c* axis (Figure 5b).

The orientation distribution figures show that a montbrayite core has the most-consistent orientation (Figure 5c). It shows no subdomains or mechanical defects, which is typical for free-growing crystals. The clusters on the pole figure of quartz have a deformational widening and are mirrored due to twinning. The pole figure of frohbergite has an array of chaotically dispersed clusters with apparent directional widening. It can indicate an obstructed growth, such as a gradual growth through a solid transition or protophase decay. Gold has the widest orientation clusters on the pole figures, which is usual for the metal due to its high ductility. It can also be a sign of the mechanical stress superimposed on the symplectites during the solid phase transformations (Figure 5c). The local misorientation distribution map confirms the data from pole figures and shows a highly deformed rim around the montbrayite core. Besides, it also shows defects in the quartz matrix located around the inclusion. These dislocations suggest a volumetric expansion of the inclusion during its evolution (Figure 5d).

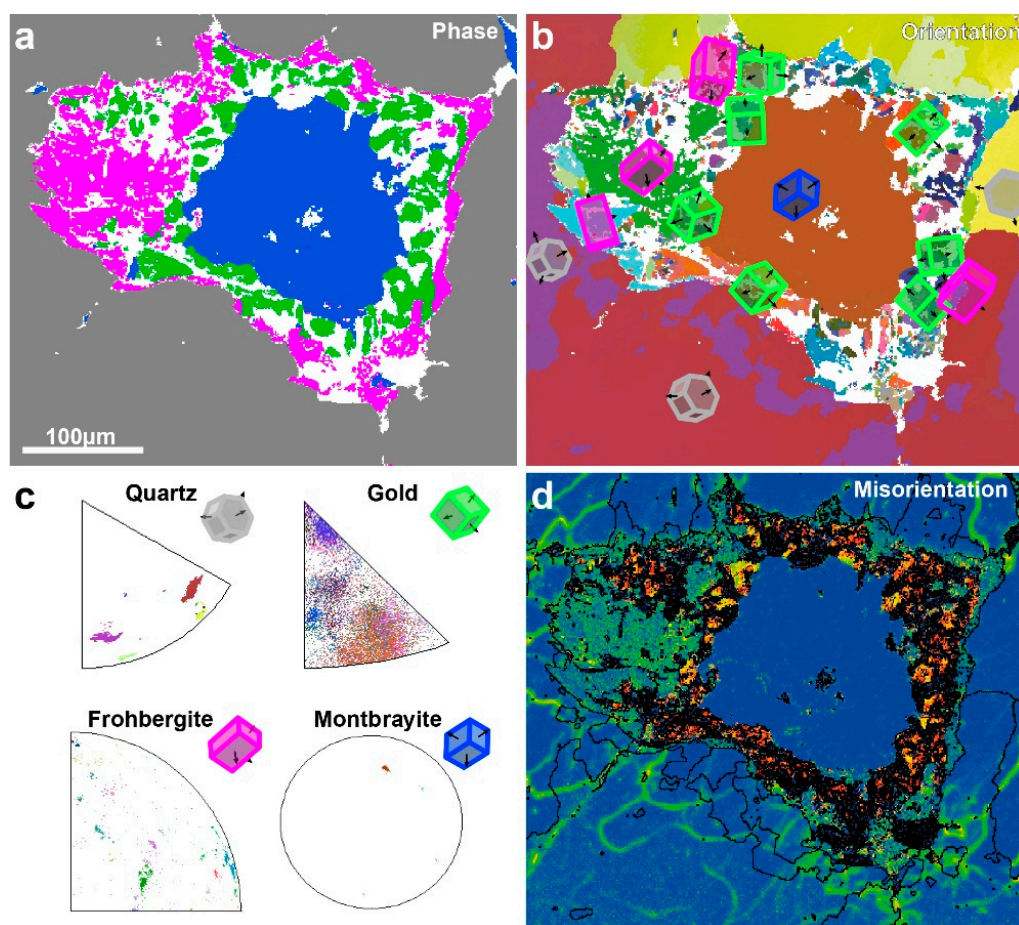


**Figure 5.** EBSD mapping of the montbrayite-containing assemblage (Grain A): (a) phase map, (b) orientation map, Euler angles color scheme, (c) inverse pole figures (y component) of the constituting map, (d) misorientation map. The white-colored area (Figure 4a) does not give Kikuchi bands.

#### 4.4. Raman Spectroscopy

This is the first Raman study of montbrayite. Representative Raman spectra using 532 nm-wavelength excitations for the selected samples are shown in Figure 6. The wavenumber positions of the bands and Raman parameters are given in Table 3. All the collected Raman spectra of montbrayite exhibit similarities and share some common features. Vibrational modes with peak positions in the range of 62–70, 87–92, 112–120, and  $\sim 302\text{ cm}^{-1}$  are present in all the spectra. The montbrayite samples exhibit a broad Raman band at about  $90\text{ cm}^{-1}$  with a halfwidth from 17 to  $38\text{ cm}^{-1}$  (Table 3, Figure 6a). This band has a greater Raman intensity in the spectra for the Grain B and other grains (Figure 6a,b,d), unlike Grain A (Figure 6b,c). The average main peak positions are 62, 99, 116, 135, 177, and  $302\text{ cm}^{-1}$  in the spectra for Grain A. Band fitting was performed using a Voigt function with the minimum number of component bands used for the fitting process (Table 3, Figure 6c,d). The structure of montbrayite is triclinic, with space group  $P\bar{1} = C_i$  [13]. There are 19 Te atoms with  $C_1$  site symmetry and two non-equivalent lattice sites for 11 Au atoms ( $C_1$  site symmetry) and 1 Au with  $C_i$  site symmetry per primitive cell in the crystal structure. As the primitive unit cell contains 61 atoms, there are 183 vibration modes, 90  $A_u$  infra-red active modes, 90  $A_g$  Raman active modes, and 3  $A_u$  acoustic modes at  $k = 0$ . The montbrayite exhibits a large number of overlapping Raman active modes. The observed features depend on both the chemical composition and the structural characteristics, including the presence of vibrations at  $k$  not equal to zero for the montbrayite structure with commensurate modulation of  $\sim 52.6\text{ \AA}$  along  $[3010]$  [13].

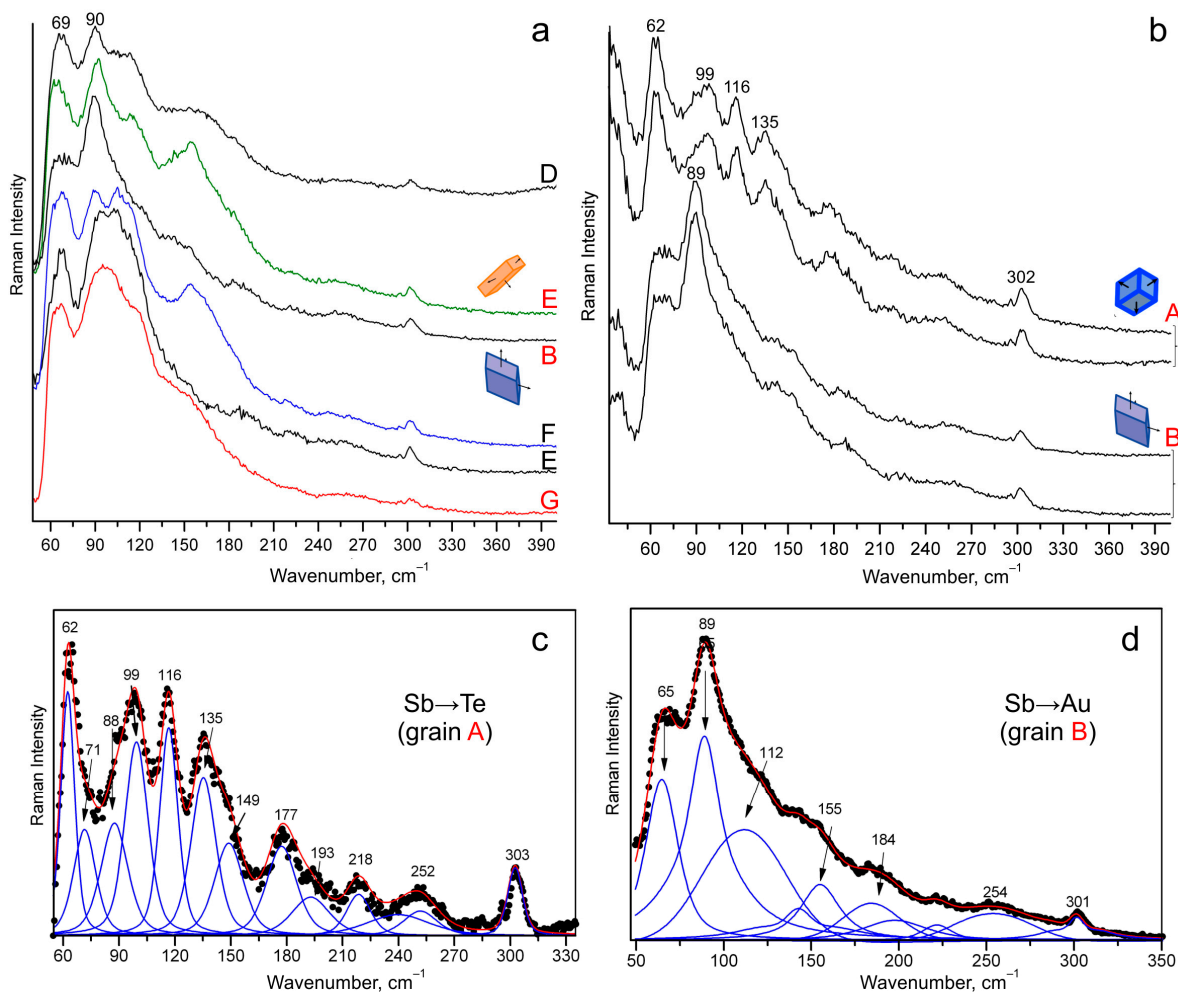


**Figure 6.** Raman spectra of montbrayite. (a,b) Raman spectra of studied grains of montbrayite are marked with capital letters; the grains with EBSD data are highlighted in red. (c,d) Band fitting of the Raman spectra of montbrayite Grains A and B with presumed various substitution mechanisms for Sb.

**Table 3.** Raman spectra parameters (band positions and full-width at half-maximum (FWHM) for each mode) of montbrayite obtained from the deconvolution of the spectra.

1	2	3	4	5	6	7	8	9	10	11	12	13	14
Peak	FWHM												
		38	5			41	9	38	29	40	13	43	10
<b>62</b>	9	<b>65</b>	22	66	24	62	12	60	8	60	8	62	11
71	14					71	13	67	15	68	15	71	10
88	17	<b>89</b>	25	<b>90</b>	17	<b>87</b>	27	<b>90</b>	17	<b>89</b>	25	<b>92</b>	38
99	15			103	25					104	13		
116	12	112	54	118	29	112	31	116	30	114	27	120	28
135	16							120	25				
149	18	142	27	146	34							148	70
		155	27			155	60	153	45	157	60		
177	19	184	38	171	18								
		198	43	190	39	190	22	185	31				
193	23	222	20	222	34	217	98	216	33	197	170		
218	15	254	50	257	53	262	30	255	52	245	68		
240	40												
279	21												
303	10	301	15	302	8	303	14	302	13	302	14	294	3

Montbrayite grains: 1, 2—A; 3, 4—B; 5, 6—C; 7, 8—D; 9, 10—E; 11, 12—F; 13, 14—G. Peaks with high intensity are highlighted in bold.

Based on the published data on other compounds of Au, Sb, Bi, Pb, and Te (see Table A2), we attempted to relate the observed Raman peaks and chemical bonds as follows: the peaks in the ranges of 88–92, 99–104, 112–120, and 135  $\text{cm}^{-1}$  likely correspond to Te–Te bonds; 38–43  $\text{cm}^{-1}$ —to Au–Te or Te–Te bonds; 60–62  $\text{cm}^{-1}$ —to Sb–Te, Au–Te, or Te–Te bonds; 66–71  $\text{cm}^{-1}$ —to Sb–Te bonds; and 153–157  $\text{cm}^{-1}$ —to Sb–Te, Sb–Sb or Au–Sb bonds. This assignment may be speculative and requires further research. All the corresponding Raman modes with references are summarized in Table A2.

## 5. Discussion

### 5.1. Chemical Variability of Montbrayite

The montbrayite from the Svetlinsk gold–telluride deposit has non-stoichiometric compositions, which are located both on the  $(\text{Au,Sb})_{23}\text{Te}_{38}$  and  $\text{Au}_{23}(\text{Te,Sb})_{38}$  stoichiometric lines. Antimony is a main impurity in the studied montbrayite, which also contains Pb, Bi, Ag, and Cu. We explain this by two substitution mechanisms for antimony in the studied montbrayite grains:  $\text{Sb} \rightarrow \text{Au}$  (2.5–5.6 wt% Sb) and  $\text{Sb} \rightarrow \text{Te}$  (7–8 wt% Sb). Grains with  $\text{Sb} \rightarrow \text{Au}$  substitution mechanism contain Ag and Cu. An inverse relationship between Sb and Ag contents was found that indirectly confirms the  $\text{Sb} \rightarrow \text{Au}$  mechanism because Ag, when present, substitutes for Au in montbrayite [13]. The mineral composition, namely the antimony content, is manifested in both the reflection and Raman spectra. The slope of the reflectance spectra decreases, and the curve in the blue–green region of the spectrum disappears with increasing of Sb content in montbrayite. In the Raman spectra, montbrayite with different Sb substitution mechanisms differs in the average positions of a peak with high intensity. They are  $\sim 64 \text{ cm}^{-1}$  and  $\sim 90 \text{ cm}^{-1}$  for montbrayite with  $\text{Sb} \rightarrow \text{Te}$  and  $\text{Sb} \rightarrow \text{Au}$ , respectively. We believe that the variations of the peak position for grains with  $\text{Sb} \rightarrow \text{Au}$  are the result of Sb substitution of Au in a disordered fashion in the mineral structure. The variability of the exhibited Raman modes also depends on the crystal orientation and was demonstrated by high-resolution Raman spectroscopy of calaverite at low temperature [29].

### 5.2. Formation Conditions of Montbrayite

Montbrayite is a rare gold telluride, the stability of which is controlled by the presence of impurities of Sb, Bi, Pb, and Ag in its structure. In nature, both Sb-rich and Bi-rich, as well as Pb-rich montbrayite have been found, e.g., [1,10,20]. We believe, however, following Bachechi [6], that the role of Sb is the main one, since the phase corresponding to montbrayite based on X-ray diffraction was synthesized only in the Au–Sb–Te system [7–9]. In the Au–Bi–Te [30,31] and Au–Pb–Te [32] systems, no ternary compounds were detected. Montbrayite from the Svetlinsk deposit is an Sb-rich variety of the mineral. Based on this, we used data from experimental studies of the ternary system Au–Sb–Te for the estimation of the possible conditions of the montbrayite formation. The eutectic assemblage  $\text{Mnb} + \text{Au} + \text{Sb}_2\text{Te}_3$  crystallizes at 423 °C, and at 444 °C, montbrayite melts with decomposition into  $\text{AuTe}_2$  and melt [7]. The peritectic temperature was estimated as 460 °C ( $\text{Mnb} - \text{AuTe}_2 + \text{melt}$ ) [8]. In studying the Au–Sb–Te system at 350 °C, the following univariant assemblages were defined: montbrayite + calaverite<sub>ss</sub> + Au, montbrayite + Au +  $\text{Sb}_2\text{Te}_3$ , montbrayite +  $\text{Sb}_2\text{Te}_3$  + calaverite<sub>ss</sub> [9]. Montbrayite was also synthesized in the temperature interval of 360–400 °C [6], and evidence for its melting at 420 and 440 °C was found. Subsequently, a melting temperature of  $410 \pm 5$  °C was estimated by a heating experiment; synthetic montbrayite (with 5.5 at% of Au substituted by Sb plus Pb and 4.0 at% of Te substituted by Bi) melts at 410 °C and does not undergo any phase transformations in the range of temperature of 200–410 °C [6]. According to these experimental data, we estimated the upper temperature range of montbrayite crystallization as 410–440 °C.

The formation temperature of chlorite coexisting with montbrayite was estimated as 349–385 °C using a chlorite geothermometer (Vikent'eva, unpublished data). The robinsonite composition from montbrayite assemblages probably suggests the high temperature of its formation ( $\sim 350$ – $370$  °C or higher), because the robinsonite composition changes to the more metal-rich side at 320 °C [33]. The study of fluid inclusions from quartz indicates that the

mineralization formed at temperatures from 365 to 240 °C, from 345 to 195 °C, and from 405 to 295 °C during 1 to 3 stages, respectively [26]. High temperatures were obtained by mineral geothermometers for early minerals from gold–telluride assemblages (pyrrhotite—375–550 °C, arsenopyrite—300–320 °C and 355–440 °C for the center and edge of the grains, respectively; Vikent'eva, unpublished data). The high-temperature formation conditions of telluride mineralization are one of the specific features of the Svetlinsk deposit [23].

### 5.3. Decomposition of Montbrayite

This study was also focused on the reaction zones rimming the montbrayite, where symplectite-like textures were observed. Two grains of montbrayite in contact with frohbergite demonstrate decomposition: (1) into native gold and Sb-bearing calaverite (Figure 1a) and (2) into native gold and tellurantimony (Figure 1b). A small amount of altaite was also found in both products' intergrowths; altaite contains a Bi impurity (see Figure 2).

Previous studies of montbrayite have shown the formation of complex intergrowths, both along the grain boundaries and inside the grains. Montbrayite from the Robb-Montbray, which was described as a new mineral, contains ovoid inclusions of the eutectoid intergrowth of tellurobismuthite and altaite [1]. Tellurantimony is intergrown with worm-shaped native gold on the contact of melonite and montbrayite from the Golden Mile [16]. Intergrowths of tellurantimony with native gold were found along the contact of montbrayite and frohbergite at the Pompas Au-U occurrence, Finland [34].

Textures similar to those observed by us can be a result of different processes. Symplectites could have been formed during the breakdown of the parent phase, its partial melting, or during the replacement of montbrayite by a coupled dissolution–reprecipitation (CDR) reaction. The main features of the replacement reactions are as follows, e.g., [35]: (1) some of the parent material is lost to the fluid phase; (2) porosity in the product phase that cannot be explained by the change in molar volume between the parent and product; (3) a sharp reaction front between the parent and product, with no significant diffusion profile in the parent. The CDR mechanism acts over a wide range of conditions, but is particularly common at low temperature when solid-state diffusional (SSD) mechanisms are less favorable. The role of these different processes was demonstrated for the decomposition of maldonite to gold and bismuth, e.g., [36,37], and for the transformation of gold tellurides in hydrothermal conditions (e.g., calaverite and krennerite to gold follow CDR reactions at 220 °C [38,39]; sylvanite to Au–Ag alloy through the complex of CDR and SSD reactions at 160–220 °C [40]).

Experimental studies have shown that montbrayite decomposed to calaverite and gold. Bachechi [6] found that the synthetic montbrayite melts at 440 °C and 420 °C, the resulting quench products being mainly calaverite and gold (however, tellurobismuthite was also identified, and Sb in variable amounts was found in the calaverite; however, altaite was not detected). Furthermore, Bachechi conducted experiments on the Au–Te system at the Au<sub>2</sub>Te<sub>3</sub> composition in the temperature range 250–440 °C. Intergrowths of calaverite and native gold were observed, but two varieties of calaverite were found, one homogeneous and the other containing numerous small particles of gold. These textures were interpreted by the author as a simultaneous growth of calaverite and metastable montbrayite, followed by a breakdown of the latter to calaverite and gold [6]. The fusion experiments by Peacock and Thompson [1] gave similar intergrowths of calaverite and gold; in the beginning, the calaverite was crystallized, and finally, a mixture of calaverite and native gold was solidified.

Taking the above into consideration, we assume the following scenario for our observed textures of montbrayite decomposition. The high-temperature formation of mineral assemblages and the composition of fluids were favorable for the crystallization of montbrayite. A local temperature increase above 410 °C led to melting with decomposition to Sb-bearing calaverite and native gold or to tellurantimony and native gold. The temperature could be lower if we consider the presence of Pb, Bi, and Ag impurities in the studied montbrayite. The volume change of montbrayite decomposition reactions was positive (see Appendix B), and thus, it is a potential cause of stresses in the matrix, which eventually leads to fracturing

both of frobergite and partly of the parent montbrayite, as well as of the quartz matrix. The subsequent inflow of fluid through the cracks leads to the leaching of calaverite, the dissolution of gold, and the precipitation of nonporous calaverite without the Sb impurity between frobergite grains, of the Au-rich phase replacing frobergite (Figures 1a and 2), and of altaite in radial cracks in the surrounding quartz. The complex history of deposit formation including two metamorphism events [23], the abundance of mineral intergrowths in ores that are typical for crystallization from melts (Vikent'eva, unpublished data), and our assumptions about polymetallic melts as an alternative mechanism of gold concentration in the Svetlinsk hydrothermal system [41] also do not contradict montbrayite melting.

## 6. Conclusions

1. Two substitution mechanisms for antimony were proposed for montbrayite from the Svetlinsk gold–telluride deposit:  $\text{Sb} \rightarrow \text{Au}$  (2.5–5.6 wt% Sb) and  $\text{Sb} \rightarrow \text{Te}$  (7–8 wt% Sb).
2. The slope of the reflectance spectra decreases, and the curve in the blue–green region of the spectrum disappears with increasing Sb content in montbrayite.
3. The average positions of the peak with high intensity are  $\sim 64 \text{ cm}^{-1}$  and  $\sim 90 \text{ cm}^{-1}$  for montbrayite with  $\text{Sb} \rightarrow \text{Te}$  and  $\text{Sb} \rightarrow \text{Au}$ , respectively. Variations of the peak position are the result of Sb substitution of Au in a disordered fashion.
4. The upper temperature range of montbrayite crystallization is 410–440 °C.
5. A possible scenario of montbrayite decomposition is as follows: local temperature increase  $\rightarrow$  montbrayite melting and decomposition  $\rightarrow$  positive volume change  $\rightarrow$  reaction-induced fracturing  $\rightarrow$  fluid inflow through cracks  $\rightarrow$  leaching of calaverite, dissolution of gold, precipitation of new phases.

**Author Contributions:** Conceptualization, O.V.V., methodology and investigation, O.V.V., V.V.S., V.D.S. and T.N.M.; field work, I.V.V. and O.V.V.; writing—original draft preparation, O.V.V.; reviewing and editing of the draft, O.V.V., V.V.S., I.V.V. and N.S.B.; project administration, N.S.B. All authors have read and agreed to the published version of the manuscript.

**Funding:** The Ministry of Science and Higher Education of the Russian Federation partially financed this research. The work was performed under the theme of state assignment of the IGEM RAS (121041500220-0) and IGM SB RAS (122041400243-9, the interpretation of Raman spectroscopic data).

**Data Availability Statement:** Not applicable.

**Acknowledgments:** We thank S.E. Borisovskiy and E.V. Kovalchuk (EMPA), O.A. Doynikova and L.O. Magazina (SEM), K. Novoselov (reflectance measurements), and M. Lozhkin (Ar ion polishing for EBSD) for carrying out the analytical procedures. We are grateful to the anonymous reviewers for their comments and suggestions. We thank the managers and geological team of JSC Uzhuralzoloto Group of Companies (UGC) for their assistance during fieldwork. V.D.S. acknowledges support from the Lomonosov Moscow State University Program of Development and thanks M.F. Vigasina for fruitful discussion of the Raman spectroscopy results. The work was performed on the state assignment of IGEM RAS and in part of IGM SB RAS.

**Conflicts of Interest:** The authors declare no conflict of interest.

## Appendix A

**Table A1.** Review of the electron microprobe analyses of montbrayite.

No.	Wt%							Formula Calculated on the Basis of 61 Atoms					
	Ag	Au	Pb	Sb	Bi	Te	Total	Ag	Au	Pb	Sb	Bi	Te
	<b>Bi-rich montbrayite</b>												
1	0.55	44.32	1.61	0.90	2.81	49.80	99.99	0.48	21.15	0.73	0.70	1.26	36.68
2	0.60	47.70	1.30	0.30	2.90	47.00	99.80	0.53	23.13	0.60	0.24	1.33	35.18
3	–	46.10	1.10	1.10	3.80	47.10	99.20	0	22.46	0.51	0.87	1.74	35.42
4	–	46.00	1.10	1.00	4.00	47.40	99.50	0	22.34	0.51	0.79	1.83	35.53

Table A1. Cont.

No.	Wt%						Formula Calculated on the Basis of 61 Atoms						
	Ag	Au	Pb	Sb	Bi	Te	Total	Ag	Au	Pb	Sb	Bi	Te
5	–	45.09	0.02	1.79	3.68	49.15	99.91	0	21.60	0	0.68	1.31	37.41
6	–	46.74	0.79		3.59	47.00	98.12	0	23.10	0.37	0	1.67	35.86
7	0.07	47.38	1.30		4.46	47.48	100.69	0.06	22.85	0.60	0	2.03	35.35
8	–	49.64	–	–	3.58	46.32	99.54	0	24.32	0	0	1.65	35.03
9	–	49.34	–	–	3.43	46.96	99.73	0	24.07	0	0	1.58	35.36
10	–	46.10	1.10	1.10	3.80	47.10	99.20	0	22.46	0.51	0.87	1.74	35.42
<b>Sb-rich montbrayite</b>													
11	–	48.73	–	5.63	1.95	42.97	99.28	0	23.59	0	4.41	0.89	32.11
12	0.92	44.86	–	3.73	1.75	49.17	100.43	0.79	21.03	0	2.83	0.77	35.58
13	–	50.76	–	5.03	1.79	46.55	104.13	0	23.38	0	3.75	0.78	33.10
14	–	49.71	–	4.94	1.90	46.20	102.75	0	23.18	0	3.73	0.84	33.26
15	–	50.60	–	–	–	49.40	100.00	0	24.33	0	0	0	36.67
16	–	47.70	–	4.90	–	45.20	97.80	0	23.20	0	3.86	0	33.94
17	0.10	47.90	–	5.00	–	44.70	97.70	0.09	23.34	0	3.94	0	33.63
18	–	48.30	–	4.60	–	46.40	99.30	0	23.13	0	3.56	0	34.30
19	–	48.60	0.40	6.40	–	46.20	101.60	0	22.69	0.18	4.83	0	33.30
20	–	49.60	–	6.00	–	45.10	100.70	0	23.47	0	4.59	0	32.94
21	–	48.00	0.30	6.10	–	47.20	101.60	0	22.35	0.13	4.59	0	33.92
22	–	47.40	0.10	6.80	–	46.40	100.70	0	22.22	0.05	5.16	0	33.58
23	–	47.90	–	6.40	0.10	47.10	101.50	0	22.30	0	4.82	0.04	33.84
24	–	47.10	–	7.40	0.10	46.00	100.60	0	22.07	0	5.61	0.04	33.27
25	–	47.10	0.20	7.50	–	45.40	100.20	0	22.19	0.09	5.72	0	33.01
26	0.10	46.90	0.10	7.10	–	46.90	101.10	0.08	21.83	0.04	5.35	0	33.70
27	–	46.71	–	8.36		43.19	98.26	0	22.27	0	6.45	0	31.79
28	–	46.06	–	6.36		46.94	99.36	0	21.81	0	4.87	0	34.31
<b>Pb-rich montbrayite</b>													
29	3.13	46.75	4.41	1.41		45.00	100.70	2.72	22.21	1.99	1.08	0	33.00
30	3.32	44.95	4.45	1.69		44.75	99.16	2.91	21.58	2.03	1.31	0	33.16
<b>Synthetic montbrayite</b>													
31	0.40	47.40	1.00	1.10	3.20	46.70	99.80	0.35	22.95	0.46	0.86	1.46	34.91
32									20.13		1.53		39.35
33		48.24		7.38		43.78	99.40	0	23.03	0	5.70	0	32.27
34		48.07		7.82		43.21	99.10	0	23.01	0	6.06	0	31.93
35		49.06		6.67		43.66	99.39	0	23.52	0	5.17	0	32.31

Notes: dash—below detection limit, blank—not analyzed. 1–5—Robb-Montbray, Quebec, Canada (1—[1], Fe trace; 2—[5]; 3–4—[18] (3–n = 5, Ag and Cu were sought, but not detected); 5—[13], n = 5; 6–7—Kochkar, South Urals, Russia (6—minimum content, 7—maximum content, n = 4, up to 0.04 wt%, and 0.12 apfu S, [19]); 8–10—noritic breccias from the Voronezhsky massif, Russia [21]; 11–14—Enasen, Sweden [17]; 15–28—Golden Mile, Western Australia (15—[14]; 16–18—[15]; 19–26—[10] (19–23—No. 2 Western lode, 24–26—Oroya lode); 27—[16], n = 15, included wt%/apfu 0.1/0.17 Fe, 0.14/0.24 Ni, 0.07/0.09 As, 28—[28], n = 17; 29–30—South Aksu, Kazakhstan [20], Cu and Hg trace, Se—below detection limit; 31—[6]; 32—[8]; 33–35—[9].

Table A2. Raman modes in montbrayite.

Raman Shift (cm <sup>-1</sup> )							Corresponding Raman Modes	References
A*	B	C	D	E	F	G		
	38		41	38	40	43	Mode at 42 cm <sup>-1</sup> of AuTe <sub>2</sub>	[29]
62			62	60	60	62	Mode at 57 cm <sup>-1</sup> of AuTe <sub>2</sub> Modes at 58 and 61 cm <sup>-1</sup> of AuAgTe <sub>4</sub> Sb-Te vibration (63 cm <sup>-1</sup> ) of Sb <sub>2</sub> Te <sub>3</sub>	[29] [42] [43]
71	65	66	71	67	68	71	Mode at 69 cm <sup>-1</sup> of Sb <sub>2</sub> Te <sub>3</sub> Mode at 71 cm <sup>-1</sup> of AuSbTe	[44] [45]

Table A2. Cont.

Raman Shift (cm <sup>-1</sup> )							Corresponding Raman Modes	References
A*	B	C	D	E	F	G		
88	<b>89</b>	<b>90</b>	<b>87</b>	<b>90</b>	<b>89</b>	<b>92</b>	Modes at 88 and 92 cm <sup>-1</sup> of AuTe <sub>2</sub> Modes at 88 and 95 cm <sup>-1</sup> of AuAgTe <sub>4</sub> Mode at 88 cm <sup>-1</sup> Mode at 90 cm <sup>-1</sup> of Te	[29] [42] [46] [47]
99		103				104	Mode at 101 cm <sup>-1</sup> of AuTe <sub>2</sub> Mode at 103 cm <sup>-1</sup> of Bi <sub>2</sub> Te <sub>3</sub> Mode at 105 cm <sup>-1</sup> of Cu-doped Sb <sub>2</sub> Te <sub>3</sub> Mode at 102 cm <sup>-1</sup> of AuAgTe <sub>4</sub> Mode at 98 cm <sup>-1</sup> of Se-rich AuTe <sub>2</sub> Mode at 98 cm <sup>-1</sup> of Bi <sub>2</sub> Te <sub>3</sub>	[29] [44] [48] [42] [49] [50]
116	112	118	112	120	114	120	Mode at 119 cm <sup>-1</sup> of AuTe <sub>2</sub> Te-Te vibration (116 cm <sup>-1</sup> ) of Sb <sub>2</sub> Te <sub>3</sub> Modes at 117 and 121 cm <sup>-1</sup> of AuSb <sub>2</sub> Mode at 120 cm <sup>-1</sup> of Bi <sub>2</sub> Te <sub>3</sub> and mode at 112 cm <sup>-1</sup> of Sb <sub>2</sub> Te <sub>3</sub> Mode at 120 cm <sup>-1</sup> of Cu-doped Sb <sub>2</sub> Te <sub>3</sub> Mode at 117 cm <sup>-1</sup> Mode at 112 cm <sup>-1</sup> of Sb <sub>2</sub> Te <sub>3</sub> Mode at 119 cm <sup>-1</sup> Mode at 120 cm <sup>-1</sup> Mode at 116 cm <sup>-1</sup> of Bi <sub>2</sub> Te <sub>3</sub> Modes 114 and 121 cm <sup>-1</sup> of AuAgTe <sub>4</sub>	[29] [43] [51] [44] [48] [46] [52] [53] [47] [50] [42]
135							Te-Te vibration (137 cm <sup>-1</sup> ) of Sb <sub>2</sub> Te <sub>3</sub> Mode at 134 cm <sup>-1</sup> of Bi <sub>2</sub> Te <sub>3</sub> Mode at 135 cm <sup>-1</sup> of Cu-doped Sb <sub>2</sub> Te <sub>3</sub> Mode at 137 cm <sup>-1</sup> Mode at 136 cm <sup>-1</sup> of Bi <sub>2</sub> Te <sub>3</sub> Modes at 132 and 134 cm <sup>-1</sup> of AuAgTe <sub>4</sub>	[43] [44] [48] [46] [50] [42]
149	142	146				148	Mode at 143 cm <sup>-1</sup> of AuTe <sub>2</sub> Mode at 147 cm <sup>-1</sup> of AuSbTe	[29] [45]
	155		155	153	157		Modes at 152 and 162 cm <sup>-1</sup> of AuTe <sub>2</sub> Sb-Te vibration (162 cm <sup>-1</sup> ) of Sb <sub>2</sub> Te <sub>3</sub> Modes at 155 and 162 cm <sup>-1</sup> of AuSb <sub>2</sub> Mode at 158 cm <sup>-1</sup> of AuAgTe <sub>4</sub> Mode at 160 cm <sup>-1</sup> of Cu-doped Sb <sub>2</sub> Te <sub>3</sub> Mode at 159 cm <sup>-1</sup> of AuSbTe	[29] [43] [51] [42] [48] [45]
177		171					Mode at 172 cm <sup>-1</sup> of AuTe <sub>2</sub> Mode at 176 cm <sup>-1</sup> of Au <sub>2.73</sub> Te <sub>6.23</sub> Se <sub>3.84</sub> Mode at 174 to 178 cm <sup>-1</sup> of synthetic Au <sub>3</sub> X <sub>10</sub> (X = Te, Se, S)	[29] [49] [49]
	184	190	190	185			Mode at 183 cm <sup>-1</sup> of PbTe	[53]
193	198					197	Mode at 206 cm <sup>-1</sup> of synthetic AuX (X = Te, Se, S)	[49]
218	222	222	217	216			Mode at 210 and 238 cm <sup>-1</sup> of synthetic AuX (X = Te, Se, S)	[49]
240	254	257	262	255	245		Sb-O vibration (251 cm <sup>-1</sup> )	[43]
279							Mode at 276 to 284 cm <sup>-1</sup> of synthetic Au <sub>3</sub> X <sub>10</sub> (X = Te, Se, S)	[49]
303	301	302	303	302	302	294	Mode at 302 cm <sup>-1</sup> of PbTe	[53]

\*—capital letters denote the studied montbrayite grains. Peaks with maximum intensity are highlighted in bold.

## Appendix B

The volume change was calculated by

$$\Delta V = 100 \times ((n_p \times V_{mp} - n_{pd} \times V_{mpd}) / n_{pd} \times V_{mpd}),$$

where  $n_p$  and  $n_{pd}$  are the number of moles of the product phase and the parent decomposition phase;  $V_{mp}$  and  $V_{mpd}$  are the molar volumes of the product and parent phases.

## References

1. Peacock, M.A.; Thompson, R.M. Montbrayite, a new gold telluride. *Am. Miner.* **1946**, *31*, 515–526.
2. Markham, N.L. Synthetic and natural phases in the system Au-Ag-Te. *Econ. Geol.* **1960**, *55*, 1148–1178.
3. Cabri, L.J. Phase relations in the Au-Ag-Te system and their mineralogical significance. *Econ. Geol.* **1965**, *60*, 1569–1606. [[CrossRef](#)]
4. Howie, F.H.; Veale, C.R. Low temperature synthesis of gold telluride. *J. Inorg. Nucl. Chem.* **1966**, *28*, 1149–1154. [[CrossRef](#)]
5. Rucklidge, J. Frobergite, montbrayite, and a new Pb-Bi telluride. *Can. Miner.* **1969**, *9*, 709–716.
6. Bachechi, F. Synthesis and stability of montbrayite,  $Au_2Te_3$ . *Am. Miner.* **1972**, *57*, 146–154.
7. Gather, B.; Blachnik, R. Das ternäre System Gold-Antimon-Tellur. *Int. J. Mater. Res.* **1976**, *67*, 395–399. [[CrossRef](#)]
8. Blachnik, R.; Gather, B. Notizen: Einige neue ternäre Goldchalkogenide. *Z. Naturforschung B* **1976**, *31*, 526–527. [[CrossRef](#)]
9. Nakamura, Y.; Ikeda, K. Isothermal phase relations in the Au-Sb-Te system at 350 °C. *Neues Jahrb. Mineral. Monatshefte* **2002**, *H6*, 276–288. [[CrossRef](#)]
10. Shackleton, J.M.; Spry, P.G. Antimony-rich montbrayite ( $(Au,Sb)_2Te_3$ ) from the Golden Mile, Western Australia, and its compositional implications. *Neues Jahrb. Mineral. Monatshefte* **2003**, *3*, 113–125. [[CrossRef](#)]
11. Bachechi, F. Crystal structure of montbrayite. *Nat. Phys. Sci.* **1971**, *231*, 67–68. [[CrossRef](#)]
12. Edenharter, A.; Bente, K.; Steins, M. Strukturuntersuchungen an Montbrayit,  $Au_2Te_3$ . *Z. Krist. Suppl.* **1991**, *3*, 63–64. (In German)
13. Bindi, L.; Paar, W.H.; Lepore, G.O. Montbrayite,  $(Au,Ag,Sb,Pb,Bi)_{23}(Te,Sb,Pb,Bi)_{38}$ , from the Robb-Montbray mine, Montbray, Québec: Crystal structure and revision of the chemical formula. *Can. Miner.* **2018**, *56*, 129–142. [[CrossRef](#)]
14. Travis, G.A. A Study of the Gold and Telluride Mineralization at Kalgoorlie, Western Australia. Master's Thesis, Imperial College, London, UK, 1966.
15. Golding, Y.L. Mineralogy, Geochemistry and Origin of the Kalgoorlie Gold Deposits, Western Australia. Ph.D. Thesis, University of Melbourne, Melbourne, Australia, 1978.
16. Mueller, A.G.; Muhling, J.R. Early pyrite and late telluride mineralization in vanadium-rich gold ore from the Oroya Shoot, Paringa South mine, Golden Mile, Kalgoorlie: 3. Ore mineralogy, Pb-Te (Au-Ag) melt inclusions, and stable isotope constraints on fluid sources. *Miner. Depos.* **2020**, *55*, 733–766. [[CrossRef](#)]
17. Nysten, P.; Annersten, H. The gold mineralization at Enasen, Central Sweden. *Geol. Foereningen I Stockh. Foerhandlingar* **1984**, *106*, 245–256. [[CrossRef](#)]
18. Criddle, A.J.; Stanley, C.J.; Paar, W.H. The optical properties of montbrayite,  $Au_2Te_3$ , from Robb Montbray, Quebec, compared with those of the other gold tellurides. *Can. Miner.* **1991**, *29*, 223–229.
19. Spiridonov, E.M. Mineralogy of the metamorphosed Kokchar plutogenic gold-quartz deposit (Southern Urals): 1. Gold-telluride ores (new minerals Bi-Pb-Te-S; kochkarite, ruklidgeite, aleksite, gold, montbrayite, tellurides and sulphides of Bi). *Proc. Russ. Mineral. Soc.* **1995**, *124*, 24–39.
20. Spiridonov, E.M. New data on mineralogy of deposits of plutogenic gold-quartz formation in the northern Central Kazakhstan. Part I. *New Data Miner.* **2014**, *49*, 57–73.
21. Genkin, A.D.; Safonov, Y.G.; Tsepin, A.I.; Scherbachev, D.K. Montbrayite from Voronezhsky Massif. *Proc. Russ. Mineral. Soc.* **1999**, *128*, 93–94.
22. Palyanova, G.A. Gold and silver minerals in sulfide ore. *Geol. Ore Dep.* **2020**, *62*, 383–406. [[CrossRef](#)]
23. Sazonov, V.N.; Popov, V.A.; Grigoryev, N.A.; Murzin, V.V.; Metsner, E.I. *Crust-Mantle Mineralisation in the Salic Blocks of Eugeosyncline*; UrO USSR AN: Sverdlovsk, Russia, 1989; 113p. (In Russian)
24. Vikent'eva, O.V.; Bortnikov, N.S. The large Svetlinsk Au-Te deposit, South Urals: Telluride mineralization for genetic reconstructions. In Proceedings of the 13th Biennial SGA Meeting, Nancy, France, 24–27 August 2015; pp. 851–854.
25. Bortnikov, N.S.; Murzin, V.V.; Sazonov, V.N.; Prokof'ev, V.Y.; Stolyarov, M.I. The Svetlinsk gold-telluride deposit, Urals, Russia: Mineral paragenesis, fluid inclusions and stable isotope studies. In Proceedings of the Fifth Biennial SGA Meeting and the Tenth Quadrennial JAGOD Symposium, London, UK, 22–25 August 1999; Volume 1, pp. 21–24.
26. Vikent'eva, O.; Prokofiev, V.; Borovikov, A.; Kryazhev, S.; Groznova, E.; Pritchkin, M.; Vikentyev, I.; Bortnikov, N. Contrasting Fluids in the Svetlinsk Gold-Telluride Hydrothermal System, South Urals. *Minerals* **2020**, *10*, 37. [[CrossRef](#)]
27. Shackleton, J.M.; Spry, P.G.; Bateman, R. Telluride mineralogy of the Golden Mile deposit, Kalgoorlie, Western Australia. *Can. Miner.* **2003**, *41*, 1503–1524. [[CrossRef](#)]
28. Mueller, A.G.; Hagemann, S.G.; Brugger, J.; Xing, Y.; Roberts, M.P. Early Fimiston and late Oroya Au-Te ore, Paringa South mine, Golden Mile, Kalgoorlie: 4. Mineralogical and thermodynamic constraints on gold deposition by magmatic fluids at 420–300 °C and 300 MPa. *Miner. Depos.* **2020**, *55*, 767–796. [[CrossRef](#)]

29. van Loosdrecht, P.H.M.; van Bentum, P.J.M.; Balzuweit, K. Raman study of incommensurately modulated calaverite (AuTe<sub>2</sub>). *Ferroelectrics* **1992**, *125*, 517–522. [[CrossRef](#)]
30. Gather, B.; Blachnik, R. Das System Gold–Wismut–Tellur. *Z. Met.* **1974**, *65*, 653–656. (In German with English Abstract) [[CrossRef](#)]
31. Winkler, E.W.; Bright, N.F.H. Experiments in the Au–Bi–Te system. *Solid State Communications* **1964**, *2*, 293–295.
32. Legendre, B.; Souleau, C. Etude du systeme ternaire Au–Pb–Te. *Bull. Chim. Fr.* **1972**, *2*, 473–479. (In French)
33. Kitakaze, A.; Nakamura, M.; Komatsu, R. Phase relation of some sulfide systems-(6): Especially Pb–Sb–S ternary system. *Mem. Fac. Eng. Yamaguchi Univ.* **2020**, *71*, 7–16.
34. Polekhovskiy, Y.S.; Petrov, S.V.; Kalinin, A.A.; Koval, A.V. New data on mineralogy of the Rompas gold-uranium occurrence, Finland. In *Proceedings of the Fersman Scientific Session; Kola Science Center RAS: Apatity, Russia, 2018; Volume 15*, pp. 482–486. (In Russian)
35. Putnis, A. Mineral replacement reactions: From macroscopic observations to microscopic mechanisms. *Miner. Mag.* **2002**, *66*, 689–708. [[CrossRef](#)]
36. Ciobanu, C.L.; Birch, W.D.; Cook, N.J.; Pring, A.; Grundler, P.V. Petrogenetic significance of Au–Bi–Te–S associations: The example of Maldon, Central Victorian gold province, Australia. *Lithos* **2010**, *116*, 1–17. [[CrossRef](#)]
37. Gamyranin, G.N.; Nekrasov, I.Y.; Samusikov, V.P. Maldonite from gold occurrences of Eastern Yakutia. *Miner. J.* **1986**, *8*, 65–71.
38. Zhao, J.; Brugger, J.; Grundler, P.V.; Xia, F.; Chen, G.; Pring, A. Mechanism and kinetics of a mineral transformation under hydrothermal conditions: Calaverite to metallic gold. *Am. Miner.* **2009**, *94*, 1541–1555. [[CrossRef](#)]
39. Xu, W.; Zhao, J.; Brugger, J.; Chen, G.; Pring, A. Mechanism of mineral transformations in krennerite, Au<sub>3</sub>AgTe<sub>8</sub>, under hydrothermal conditions. *Am. Miner.* **2013**, *98*, 2086–2095. [[CrossRef](#)]
40. Zhao, J.; Brugger, J.; Xia, F.; Ngothai, Y.; Chen, G.; Pring, A. Dissolution-precipitation vs. solid-state diffusion: Mechanism of mineral transformations in sylvanite, (AuAg)<sub>2</sub>Te<sub>4</sub>, under hydrothermal conditions. *Am. Miner.* **2013**, *98*, 19–32. [[CrossRef](#)]
41. Vikent'eva, O.V.; Bortnikov, N.S. Evidences of mineral melting in the ores of the Svetlinsk gold deposit, South Urals, Russia. *Dokl. Earth Sci.* **2023**, *513*, 2.
42. Amiel, Y.; Kafle, G.P.; Komleva, E.V.; Greenberg, E.; Ponomov, Y.S.; Chariton, S.; Lavina, B.; Zhang, D.; Palevski, A.; Ushakov, A.V.; et al. Sylvanite AuAgTe<sub>4</sub>: A rare case of gold superconducting material. *J. Mater. Chem. C* **2023**, *11*, 10016. [[CrossRef](#)]
43. Zybala, R.; Mars, K.; Mikula, A.; Boguslawski, J.; Soboń, G.; Sotor, J.; Schmidt, M.; Kaszyca, K.; Chmielewski, M.; Ciupiński, L.; et al. Synthesis and characterization of antimony telluride for thermoelectric and optoelectronic applications. *Arch. Metall. Mater.* **2017**, *62*, 1067–1070. [[CrossRef](#)]
44. Richter, W.; Köhler, H.; Becker, C.R. A Raman and far-infrared investigation of phonons in the rhombohedral V<sub>2</sub>–VI<sub>3</sub> compounds Bi<sub>2</sub>Te<sub>3</sub>, Bi<sub>2</sub>Se<sub>3</sub>, Sb<sub>2</sub>Te<sub>3</sub> and Bi<sub>2</sub>(Te<sub>1–x</sub>Se<sub>x</sub>)<sub>3</sub> (0 < x < 1), (Bi<sub>1–y</sub>Sb<sub>y</sub>)<sub>2</sub>Te<sub>3</sub> (0 < y < 1). *Phys. Stat. Sol.* **1977**, *6*, 619–628.
45. Vikent'eva, O.V.; Shilovskikh, V.V.; Shcherbakov, V.D.; Vikentyev, I.V.; Bortnikov, N.S. A Rare Au–Sb telluride pampaloite from the Svetlinsk gold-telluride deposit, South Urals, Russia. *Minerals* **2022**, *12*, 1274. [[CrossRef](#)]
46. Rodríguez-Fernández, C.; Manzano, C.V.; Romero, A.H.; Martín, J.; Martín-González, M.; Morais de Lima Jr, M.; Cantarero, A. The fingerprint of Te-rich and stoichiometric Bi<sub>2</sub>Te<sub>3</sub> nanowires by Raman spectroscopy. *Nanotechnology* **2016**, *27*, 075706. [[CrossRef](#)]
47. Volodin, V.A.; Sinyukov, M.P.; Shcheglov, D.V.; Latyshev, A.V.; Fedosenko, E.V. Raman scattering in PbTe and PbSnTe films: In situ phase transformations. *Semiconductors* **2014**, *48*, 173–177. [[CrossRef](#)]
48. Shi, D.; Wang, R.; Wang, G.; Li, C.; Shen, X.; Nie, Q. Enhanced thermoelectric properties in Cu-doped Sb<sub>2</sub>Te<sub>3</sub> films. *Vacuum* **2017**, *145*, 347–350. [[CrossRef](#)]
49. Palyanova, G.; Beliaeva, T.; Kokh, K.; Seriotkin, Y.; Moroz, T.; Tolstykh, N. Characterization of synthetic and natural gold chalcogenides by electron microprobe analysis, X-ray powder diffraction, and Raman spectroscopic methods. *J. Raman Spectrosc.* **2022**, *53*, 1012–1022. [[CrossRef](#)]
50. Russo, V.; Bailini, A.; Zamboni, M.; Passoni, M.; Conti, C.; Casari, C.S.; Li Bassi, A.; Bottani, C.E. Raman spectroscopy of Bi–Te thin films. *J. Raman Spectrosc.* **2008**, *39*, 205–210. [[CrossRef](#)]
51. Freund, G.A.; Kirby, R.D.; Sellmyer, D.J. Raman scattering from pyrite structure AuSb<sub>2</sub>. *Solid State Commun.* **1977**, *22*, 5–7. [[CrossRef](#)]
52. Goncalves, L.M.; Alpuim, P.; Rolo, A.G.; Correia, J.H. Thermal co-evaporation of Sb<sub>2</sub>Te<sub>3</sub> thin-films optimized for thermoelectric applications. *Thin Solid Film.* **2011**, *519*, 4152–4157. [[CrossRef](#)]
53. Zhang, B.; Cai, C.; Zhu, H.; Wu, F.; Ye, Z.; Chen, Y.; Li, R.; Kong, W.; Wu, H. Phonon blocking by two dimensional electron gas in polar CdTe/PbTe heterojunctions. *Appl. Phys. Lett.* **2014**, *104*, 161601. [[CrossRef](#)]

**Disclaimer/Publisher's Note:** The statements, opinions and data contained in all publications are solely those of the individual author(s) and contributor(s) and not of MDPI and/or the editor(s). MDPI and/or the editor(s) disclaim responsibility for any injury to people or property resulting from any ideas, methods, instructions or products referred to in the content.